Available online at www.sciencedirect.com

SciVerse ScienceDirect

Ceramics International 39 (2013) 5467–5476

CERAMICS INTERNATIONAL

www.elsevier.com/locate/ceramint

Spark plasma sintering of ZrC–SiC ceramics with $LiYO_2$ additive

Ljiljana Kljajević[a,*], Snežana Nenadović[a], Miloš Nenadović[b], Devendraprakash Gautam[c], Tatjana Volkov-Husović[d], Aleksandar Devečerski[a], Branko Matović[a]

[a]*Laboratory for Material Science, Institute of Nuclear Sciences "Vinča", University of Belgrade, Belgrade, Serbia*
[b]*Laboratory for Atomic Physics, Institute of Nuclear Sciences "Vinča", University of Belgrade, Belgrade, Serbia*
[c]*Nanoparticle Process Technology, Department of Engineering Sciences, University of Duisburg–Essen, Lotharstrasse 1, MA 343, D-47057 Duisburg, Germany*
[d]*Faculty of Technology and Metallurgy, University of Belgrade, Belgrade, Serbia*

Received 24 September 2012; received in revised form 5 December 2012; accepted 14 December 2012
Available online 28 December 2012

Abstract

Spark plasma sintering (SPS) of ZrC–SiC composite powders in the presence of $LiYO_2$ sintering additive was studied. The starting powders were obtained by a carbothermal reduction (CTR) of natural mineral zircon ($ZrSiO_4$), which provided an intimate mixing of *in-situ* created ZrC and SiC powders. This composite powder and $LiYO_2$ as additive were densified by spark plasma sintering. Microstructural features of the composite were investigated by XRD, SEM/EDS and AFM analysis. The sintered composite material possesses promising mechanical properties and excellent cavitation resistance which was observed with a cavitation erosion test. The values of Vickers microhardness and fracture toughness of the composite material are 20.7 GPa and 5.07 $MPam^{1/2}$, respectively.

Keywords: A. Sintering; B. Composites; D. Carbides; E. Structural applications

1. Introduction

Zirconium carbide (ZrC) is one of the refractory transition metal carbides that possesses high melting point (~3693 K), high hardness (25.5 GPa), high electrical conductivity ($78 \times 10^{-6}\ \Omega$ cm) and high modulus of elasticity (440 MPa) [1]. Therefore, ZrC compound is a promising candidate for many applications such as field emitters, coating of nuclear particle fuels and ultrahigh-temperature applications [2,3]. However, the use of a single-phase material for high temperature structural application has poor mechanical resistance and oxidation tolerance. The adoption of composite approach in order to improve the properties of a single-phase ceramics has been successfully demonstrated. For example, the addition of a second phase, such as silicon carbide (SiC) in ZrC results in a composite with improved resistance to oxidation, thermal shock and ablation [4,5]. Furthermore, SiC is an important structural material owing to its unique combination of properties, such as high temperature strength, thermal shock resistance and wear and corrosion resistance [6]. It was reported that addition of SiC limits the grain growth during densification and improves the sinterability of zirconium diboride as well as enhances the strength, ablation and oxidation resistance [7].

The use of ZrC and SiC in engineering applications has been limited by the lack of commercially viable sintering techniques. High sintering temperature and external pressure are normally required to obtain dense bodies, due to highly covalent bonding character and low self-diffusion coefficients of ZrC and SiC [8,9]. One of the promising approaches for improving the densification is the use of a pulsed electric current sintering technique also referred as spark plasma sintering (SPS). This technique employs a pulsed DC current to activate and improve the sintering kinetics. High density, refined microstructure, elimination of grain boundary as well as surface impurities that have

*Corresponding author. Tel.: +381113408705.
E-mail address: ljiljana@vinca.rs (L. Kljajević).

0272-8842/$ - see front matter © 2012 Elsevier Ltd and Techna Group S.r.l. All rights reserved.
http://dx.doi.org/10.1016/j.ceramint.2012.12.058

been reported, normally result in an overall improvement in the materials' properties [10]. The SPS process is therefore particularly attractive for industrial applications of hardly sinterable ceramics [11].

The SPS method is relatively a new sintering technique that allows preparation of fully dense samples at temperature considerably lower than that used in conventional sintering methods such as pressureless sintering, hot pressing, and hot isostatic pressing. It is also important to stress that the sintering time for SPS is normally few minutes, which is much shorter compared to conventional methods where it can be up to several hours [12].

In the present work, the SPS of composite powders, synthesized by a carbothermal reduction (CTR) of natural mineral zircon, with $LiYO_2$ as an additive was studied.

The $LiYO_2$ additive was already used in comparison to mixtures of lithia and yttria, which have been effective single-component additives [13] and it offers several advantages. For example, it is less susceptible to hydrolysis and has a lower vapor pressure than Li_2O. The use of $LiYO_2$ leads to high relative densities and lower weight loss, when compared to the samples sintered with $Li_2O+Y_2O_3$ mixture. The difference in sintering behavior occurs because of the heterogeneity of the liquid phase formed in the $Li_2O+Y_2O_3$ mixture-containing samples [14]. Some reports on the use of Li_2O–Y_2O_3 as sintering additives for AlN exist in the literature [15]. Thus, $LiYO_2$ additive might be a good sintering aid for sintering ZrC–SiC ceramic materials. However, no study has been yet reported on SPS of composite material ZrC–SiC using $LiYO_2$ as a sintering additive.

The objective of this research is to evaluate the suitability of SPS in sintering of ZrC–SiC ceramics with $LiYO_2$ as additive. The results of X-ray diffraction (XRD) phase analysis, microstructure/chemical analysis using scanning electron microscope (SEM/EDS), atomic force microscope (AFM) and mechanical properties such as indentation fracture toughness and Vickers hardness are presented. Also, the cavitations erosion testing was accomplished utilizing the recommended standard.

2. Materials and methods

Commercially available zircon powder ($ZrSiO_4$, "Trebol", USA, ~40 μm) was used as the starting material. The chemical analysis of the powder, given by the manufacturer, is as follows: ZrO_2–65%, SiO_2–33%, Al_2O_3–2%, TiO_2–0.35%, Fe_2O_3–0.05%. Activated carbon (AC) dried at 383 K (2 h) was used as a reducing agent ("Trayal", Serbia, ~10 μm, ashes ≤1%, specific surface area BET ~1000 $m^2 g^{-1}$). The $C/ZrSiO_4$ mixtures were prepared by mixing $ZrSiO_4$ with an appropriate amounts of AC in order to obtain samples with a molar ratio $C/ZrSiO_4=7$. The reason for this molar ratio is explained elsewhere [16]. By varying $C/ZrSiO_4$ ratio, it is possible to obtain ZrO_2, ZrO_2/SiC or ZrC/SiC as the reaction products. SiC content increases with increasing carbon content, and reaches a maximum in the sample with 7:1 M ratio.

2.1. Preparation of composite powder

Composite powder was obtained by CTR of $C/ZrSiO_4=7$ sample at 1600 °C with a heating rate of 5 °C/min, 1 h soaking time and under 10^{-3} mbar vacuum, using a high temperature vacuum tube furnace (1600X, MTI Corporation, Santa Barbara, CA, USA).

2.2. Synthesis of $LiYO_2$

$LiYO_2$ was synthesized by mixing Y_2O_3 and Li_2CO_3 powders (Merck, Germany) and calcining at 1400 °C for 4 h with molar ratio of $Li_2CO_3/Y_2O_3=1.02$. The XRD phase analysis of the calcined material confirmed that the powder was single-phase $LiYO_2$.

2.3. Preparation of the SPS composite

The mixture of composite powder (product of CTR with molar ratio of $C/ZrSiO_4=7$) and 7.5 wt% $LiYO_2$ was sintered by the SPS technique. The amount of $LiYO_2$ added as a sintering aid, was determined on the basis of our previous studies [14,17]. As 15 wt% of $LiYO_2$ was found to be an optimum for pressureless sintering of high melting point covalent compounds such as Si_3N_4, it was supposed that in the SPS process – significantly lower amount of additive will be required. The SPS equipment FCT HP D5 (FCT Systeme GmbH, Raunstein, Germany) was used for sintering. The mixture was loaded into the graphite dies with an inner diameter of 20 mm (outer diameter 45 mm; height 50 mm). A boron nitride (BN) coated graphite foil was used to avoid the contact of the powder with the inner surface of the dies. This ensures that the current flows through the powder and not through the dies during sintering. To avoid the radial temperature distribution in the graphite dies and to minimize the radiation heating losses the dies were covered with graphite wool (the graphite wool is high quality high temperature material delivered from FCT GmbH; all the parts of dies are also delivered by FCT GmbH, Germany). The sample was heated-up by a pulsed electric current with a heating rate of 100 °C/min up to 1200 °C with a hold time of 3 min. After that the temperature was further raised with a heating rate of 100 °C/min to 1600 °C with 3 min holding time. A pressure of 35 MPa was applied on the sample over the complete heating cycle. The specimen was cooled down to 500 °C with a cooling rate of 100 °C/min with continuous releasing of the pressure. The sample was furnace cooled to the room temperature. The complete sintering was done under vacuum of 100 Pa (1 mbar). The temperature was measured with an optical pyrometer focused on the surface of the graphite push–punch.

2.4. Characterization of the SPS composite

The density of spark plasma sintered composite was measured by the Archimedes' principle (water displacement).

The fracture toughness (K_{Ic}) was determined by using the indentation method (8 Vickers indentations). Eq. (1) valid for a semi-circular crack system [18] was used to calculate K_{Ic} from the lengths of edge cracks and indentation diagonals:

$$K_{IC} = 0.016 \times \sqrt{\frac{E}{H}} \times \frac{F}{L^{1.5}} \quad (1)$$

where E=Young's modulus, 56.59 GPa, H=Vickers hardness (GPa), F is load (N), L=crack length (μm).

From the same experiments, the hardness was calculated as given below

$$H = 1.8544 \times \frac{F}{{d_H}^2} \quad (2)$$

where d_H=diagonals of the Vickers indentation (μm).

The value of Young's modulus (E) is determined on the basis measurement of ultrasonic velocity was performed using the equipment OYO model 5210 according to the standard testing procedure (SRPS D. B8. 121. former JUS. D. B8. 121.) [19].

Phase identification was carried out by a Siemens D-500 XRD powder diffractometer with Cu-K_α radiation (in conjunction with Cu-K_β nickel filter). The diffraction data were collected within $10-80^\circ$ 2θ range in steps of 0.05°, and a scan time of 2 s per step.

The microstructure and elemental analysis of the sintered material were performed on Au-coated samples using a VEGA TS 5130 mm TESCAN SEM/EDS equipment.

The surface morphology of the composite materials was quantified using AFM. The AFM studies were carried out on a Veeco MultiMode Quadrex IIIe in the tapping mode, where a cantilever was tapping the surface and gave the topography by interaction. The cantilever type is a standard RTESP-Veeco production. The tip material is 0.5–2 Ω cm phosphorus doped Si. The solid phase AFM imaging was performed in a tapping mode with a 15–20 μm high pyramidal tip. Tapping mode AFM was used to acquire surface topography images, while simultaneously recorded phase AFM images were used to detect and quantify the changes in surface chemical composition. The resonance frequency of tip was 268.2 kHz. The scan rate was maintained at 2 Hz to get an optimal image quality. During the tapping mode, it was very important to avoid thermal drift, which was manifested with lines and bad shapes over the image. For the phase image analysis, Vecco software package was used.

Phase imaging AFM technique is based on the measurement of the difference between the phase angle of the excitation signal and the phase angle of the cantilever response, which is used to map the compositional variations in heterogeneous samples [20]. This phase shift can be interpreted as maps of energy dissipation [21]. A relationship has been established between a phase shift and elastic properties for several tip–sample interactions: Elastic interaction, viscous interaction, adhesion as well as other factors [22]. Alternatively, the measurement of the phase lag of the cantilever oscillation with respect to the excitation force contains information about the interaction between the tip and the sample, allowing compositional contrast on heterogeneous surfaces. Despite the complexity of the interaction and its effect on the cantilever dynamics, theoretical simulations and experiments of the cantilever dynamics in air have shown that phase contrast arises from differences in the energy dissipation between the tip and the sample [23].

2.4.1. Cavitation erosion testing

The fluid dynamic system of the cavitations erosion methodology used here to produce ultrasonic cavitations is explained in detail elsewhere [24].

The cavitation erosion testing was conducted utilizing the recommended standard values:

- Frequency of the vibration: 20 ± 0.2 kHz.
- Amplitude of the vibration at the top of the transformer: 50 ± 2 μm.
- Gap between the test specimen and the transformer: 5.0 mm.
- Temperature of water in the bath: 25 ± 1 °C.

These parameters were controlled throughout the testing process [25–32]. The test specimen was placed under the transformer with a gap of 4.0 mm. The evaluation of the mass losses of the test specimens was done on an analytical balance with an accuracy of ± 0.1 mg. The measurements were performed after each test specimen subjected to the cavitations for 30 min. The maximal duration of the tests could be 3 h. In our testing maximal time was 150 min, and samples were controlled after 15 min. In this article the results after every 30 min will be presented. The optical microscopy was employed to analyse the effect of the erosion and to interpret the results of cavitations erosion tests.

3. Results and discussions

The phase composition of ZrC–SiC composite powder obtained after the CTR reaction of $C/ZrSiO_4 = 7$ mixture at 1600 °C and SPS synthesized composite material is shown in Fig. 1. The reflections originating from ZrC and SiC phase are clearly observed in both composite powder and the sintered material. The difference between these two patterns is the peaks that occurs at $2\theta = 29.99^\circ$; 34.79; 50.03°; 60.10°. It was found that these peaks originate from the yttria stabilized cubic zirconium oxide–$92ZrO_2$ $8Y_2O_3$ (JCPDS No. 30-1468; in some versions of XRD databases, under this card number, this compound is represented as $Y_{0.15}Zr_{0.85}O_{1.93}$). Yttria stabilized cubic zirconium oxide has probably been formed as a result of oxidizing of ZrC with $LiYO_2$ additive. $LiYO_2$

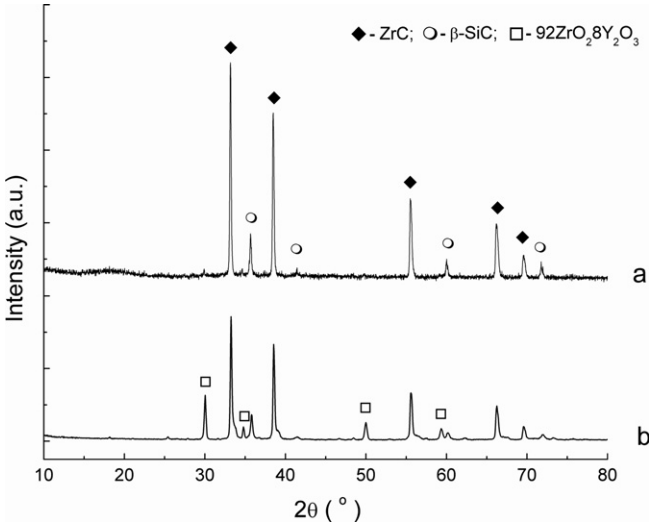

Fig. 1. Room temperature XRD patterns of: (a) ZrC–SiC composite powder; (b) SPS composite material.

degradation, accompanied with Li evaporation (due to its high vapor pressure at high temperatures such as 900 °C [33]), can be written as follows:

$$LiYO_2 \rightarrow Y_2O_3 + 2Li(\uparrow) + 1/2O_2(\uparrow) \quad (3)$$

The liberated oxygen could react with ZrC according to reaction:

$$ZrC + 2O_2 = ZrO_2 + CO_2 \quad (4)$$

However, in the present multiphase system, the potential chemical reactions can be rather complex and numerous. For example: it is also possible that SiC reacts with $LiYO_2$ and produce SiO_2; SiO_2 can further react with $LiYO_2$ and produce LiO_2–SiO_2 eutectic (m.p. = 1225 °C [14]). And additionally, all these possible reactions are compounded by the inhomogeneous local concentration of the reactants and by different local situation, regarding pressing and the presence of a gas or liquid phase.

3.1. Microstructure analysis

Results of the SEM/EDS analysis for composite powder obtained by CTR at 1600 °C, are illustrated in Fig. 2 and Table 1.

As seen, the composite powder consists of very fine particles sintered together into large agglomerates (Fig. 2c). The results of EDS elemental analysis are presented in Table 1.

Carbon content was not measured since we used the carbon adhesive tape to fix the powder on the metal carrier.

EDS results for two large areas shown in Fig. 2a and b, represent average chemical composition of the investigated area of sample. In essence, EDS results confirmed our previous observations made on the basis of XRD analysis that much higher Zr content corresponds with dominant ZrC phase in the XRD pattern (Fig. 1) and presence of Al-traces is due to Al presence in the starting $ZrSiO_4$ material.

Table 2 depicts the elementary analysis of the whole area of sintered composite material ($\sim 100 \times 100$ μm), which is shown above (see Fig. 3). The results confirmed the presence of Si, C, Zr, Y, O elements that are constituents of the compounds identified by XRD analysis.

SEM micrographs of the cross section of the composite material illustrated in Fig. 4 demonstrate that grains are very different in shape and size. Fig. 5 shows micrographs of the polished and chemically etched composite material where the presence of different phases can be noticed.

The matter transport during the SPS process is supposedly enhanced by a high current flow. The high-energy electrical pulses generate large heat dissipation at the powder particle boundaries, promoting transfer of the material that facilitates neck formation among the particles and local grain growth. The contact between ZrC and SiC particles and $LiYO_2$ additive in the presence of high energy electric pulses could drive the formation of a liquid or gas phase resulting in the cooling of the nanostructure solid phase of composite material.

Fig. 6 scan size 5×5 μm is a macroscopic representation of the surface of sintered sample. Fig. 6a presents a topographical analysis, while Fig. 6b represents the phase image of the same area. Topographic image gives information on the surface roughness, which is a consequence of the sintering process. At the phase image are noticeable areas lighter and darker colors, indicating the existence of two distinct phases. Fig. 7a and b shows the topographic and phase image scan size of 2×2 μm. On this figure are visible the additive inclusions that was used during the sintering process.

Fig. 8a and b shows the topographic and phase image scan size of 150×150 nm. Unlike Fig. 6b which clearly shows the difference between two phases Fig. 8b can not distinguished the phases. At this level of magnification, although image is not very clear, it may suggest formation of necks connecting the two grains which are marked at several points by black arrows (Fig. 8b). Some grains of single phase are 10–15 nm in diameter.

The AFM analysis of the surface composition of the SPS composite shows that the optimum magnification in this case is 5×5 μm.

An insight into the phase composition change can be obtained from AFM phase images, by generating phase distribution. A single peak is a characteristic of a homogeneous surface, while in the case of non-homogeneity two or more peaks appear [34]. Fig. 9 shows that at 5×5 μm magnifications, there are two pronounced peaks, which represent two phases in the system. The interaction of AFM microscope tip with the sample results in a change in its frequency of the oscillation, while the tip scans the inhomogeneous phase area. The change in frequency of the oscillations is given in volts and is inversely proportional

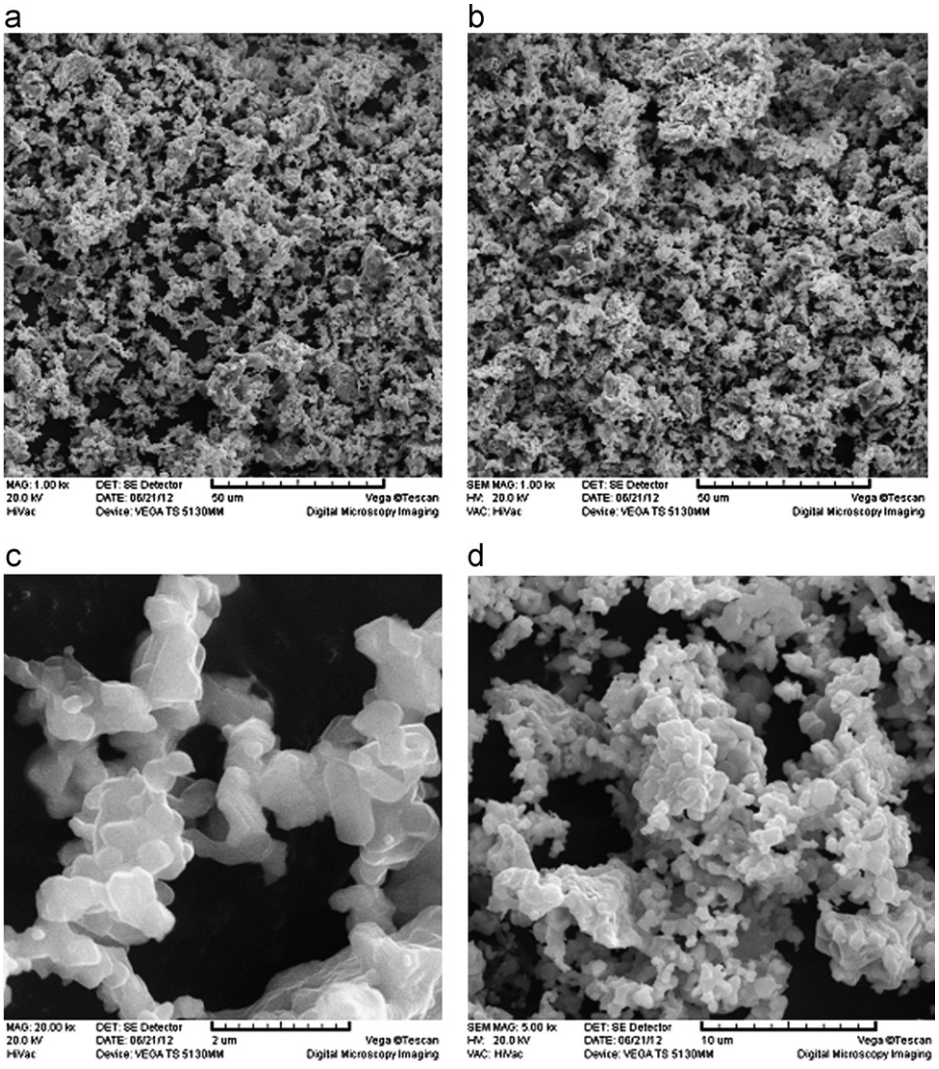

Fig. 2. SEM images of the composite powder.

Table 1
EDS analysis of composite powder.

Figure	Element (wt%)				Area scanned:
	O	Al	Si	Zr	
Fig. 2a	3.74	0.59	12.90	82.77	Whole area
Fig. 2b	3.12	0.7	13.86	82.33	Whole area

Table 2
EDS analysis of the SPS composite.

Element (wt%)					
C	O	Al	Y	Si	Zr
26.28	8.98	0.74	1.86	6.64	55.50

to the hardness of the tested material. The AFM phase spectroscopy can distinguish two or more material by difference in the coefficient of viscosity. In general, softer material leads to a larger contact area and the longer duration of tip–sample contact than those for hard material. For this reason the presence of soft material causes larger phase shift than that for hard material [35]. The peak located at low values of the phase shift indicates a harder material while the peak located at high values of the phase shift indicates a softer material. The ratio of the areas under the peaks gives the relative ratio that is consistent with the composition of the scanned surface of the examined material.

The relative amount of ZrC and SiC phase in the SPS composite surface, calculated from the Fig. 9, gives 80.64% ZrC phase and 19.36% SiC phase. Figure 5×5 μm is taken into consideration for the best agreement with the assumed stoichiometry. The reason for this assertion is that the larger area being analyzed, the greater is the accuracy of the composition. More different scans were taken for magnification of 5×5 μm from various positions and one of they was chosen. However, this is the composition of one, the best and representative 5×5 μm area of the sample.

In order to obtain accurate overall composition of the sample it is important to conduct a sufficient number of similar scans of different areas.

From the XRD (Fig. 1) and EDS measurements, we know that Y is present in the SPS composite in the form of yttria stabilized cubic zirconium oxide ($92ZrO_2 8Y_2O_3$). Since AFM analysis did not show the third phase, it is possible that during the reaction between ZrC and $LiYO_2$, $92ZrO_2 8Y_2O_3$ phase is formed on the surface of the ZrC grains

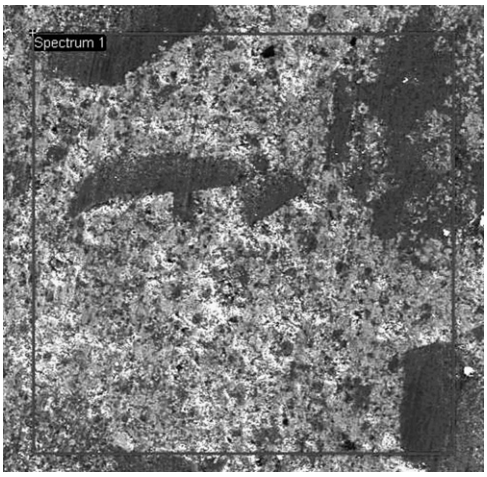

Fig. 3. SEM micrograph of whole area (~100 × 100 μm) of SPS composite used in EDS analysis.

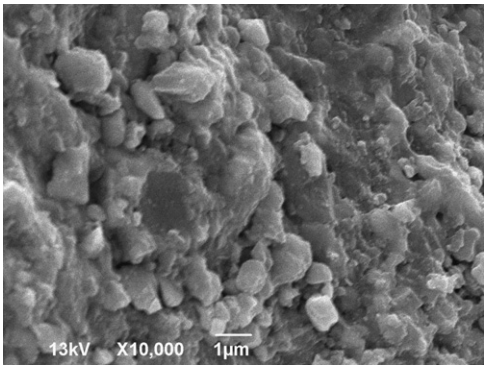

Fig. 4. Cross section micrographs of etched composite material.

3.2. Mechanical properties

The density of composite material obtained by the SPS process was measured by the Archimedes' principle is 4.70 g/cm^3. The fracture toughness (K_{IC}) and Vickers microhardness (HV) values of the composite calculated by using Eqs. (1) and (2), are 5.07 MPam$^{1/2}$ and 20.7 GPa, respectively. Since the fracture toughness of monolithic ZrC is relatively low, about 4.0 MPam$^{-1/2}$ [36], it can be concluded that the addition of SiC is an effective way to obtain ZrC–SiC composite with improved fracture toughness. The values of hardness and fracture toughness are in very good agreement with the published data [37].

The mass loss during the cavitation erosion experiment is illustrated in Fig. 10. The data shows that the sample exhibited excellent resistance to the erosion cavitation testing. The mass loss was minimal about 0.0016 g (0.06 wt%) after 150 min of testing.

The images (macrophotographs) of the sample surface during the testing are exhibited in Fig. 11, for different exposure time and also at the beginning of the experiment ($t=0$ min). After 120 min of testing, some small defects can be noticed under the optical microscope. Considerable erosion was not detected even after 150 min. The images in Fig. 11 show that the surface of the sample remains practically unchanged. These results were expected considering the results of the mass loss during the testing.

4. Conclusions

Spark plasma sintering of ZrC–SiC composite powder with $LiYO_2$ as sintering additive was successfully performed. The values for Vickers microhardness HV and fracture toughness K_{IC} of the SPS composite material are 20.7 GPa and 5.07 MPam$^{1/2}$, respectively.

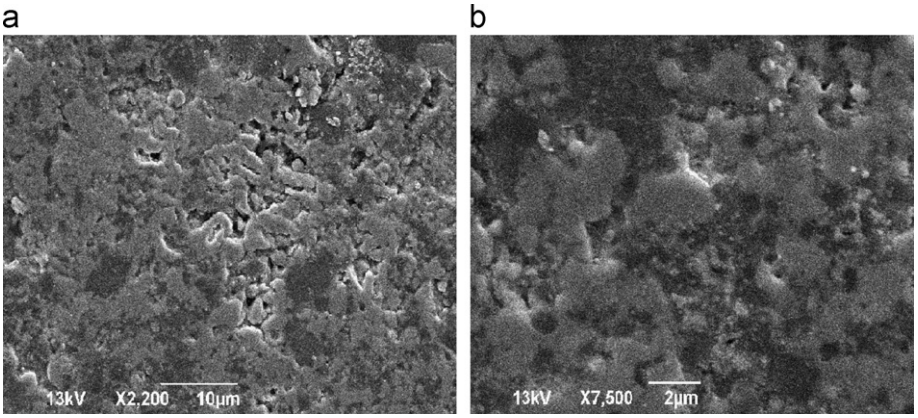

Fig. 5. Micrographs of polished and chemical etched composite material.

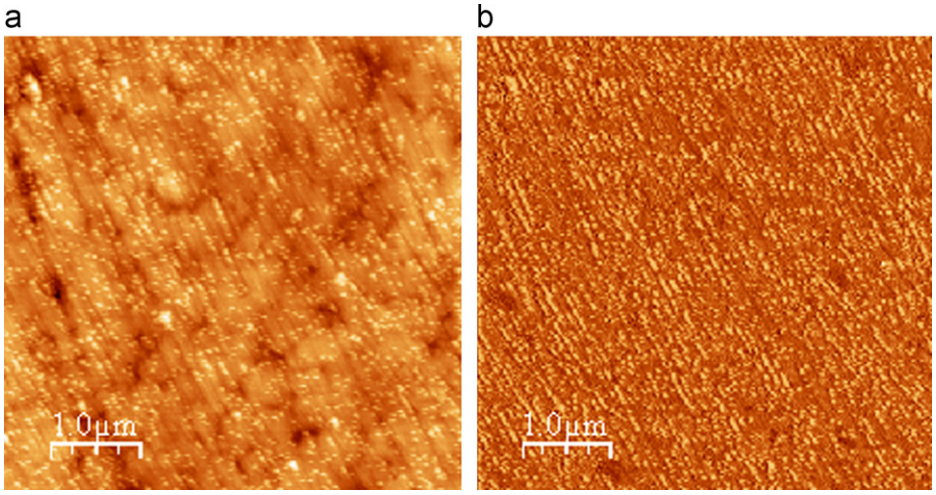

Fig. 6. AFM 5 × 5 μm images of the SPS composite: (a) topography, (b) phase composition.

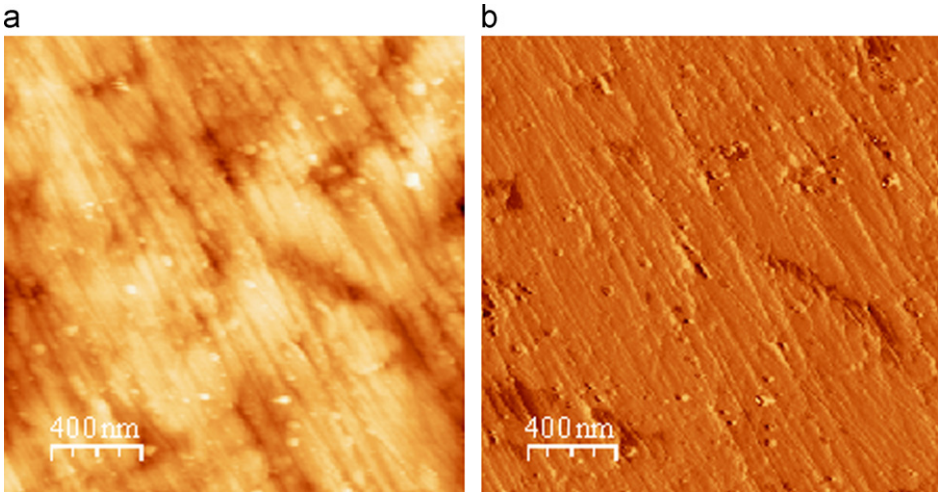

Fig. 7. AFM 2 × 2 μm images of the SPS composite: (a) topography, (b) phase composition.

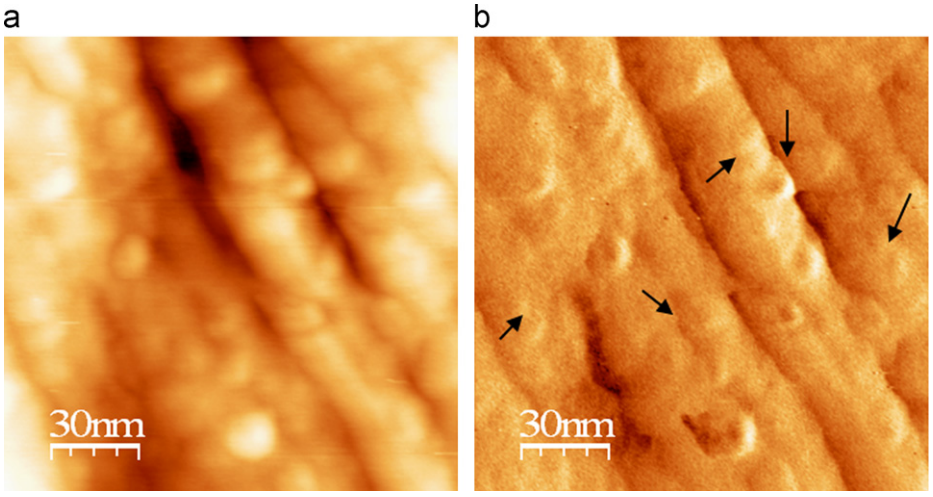

Fig. 8. AFM 150 × 150 nm images of the SPS composite: (a) topography, (b) phase composition.

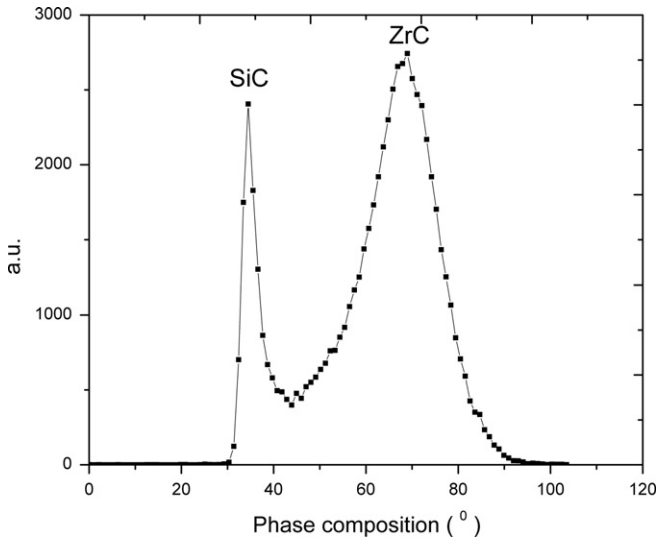

Fig. 9. AFM phase composition obtained from the 5 × 5 μm image of the SPS composite.

The AFM analysis of the surface composition of the SPS composite shows that the material is homogeneously distributed and consists of two phases. The grains of the composite material are about 10–15 nm in diameter.

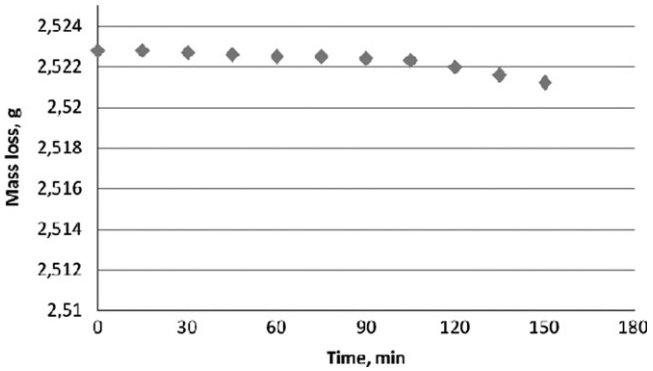

Fig. 10. Mass loss during cavitation erosion test.

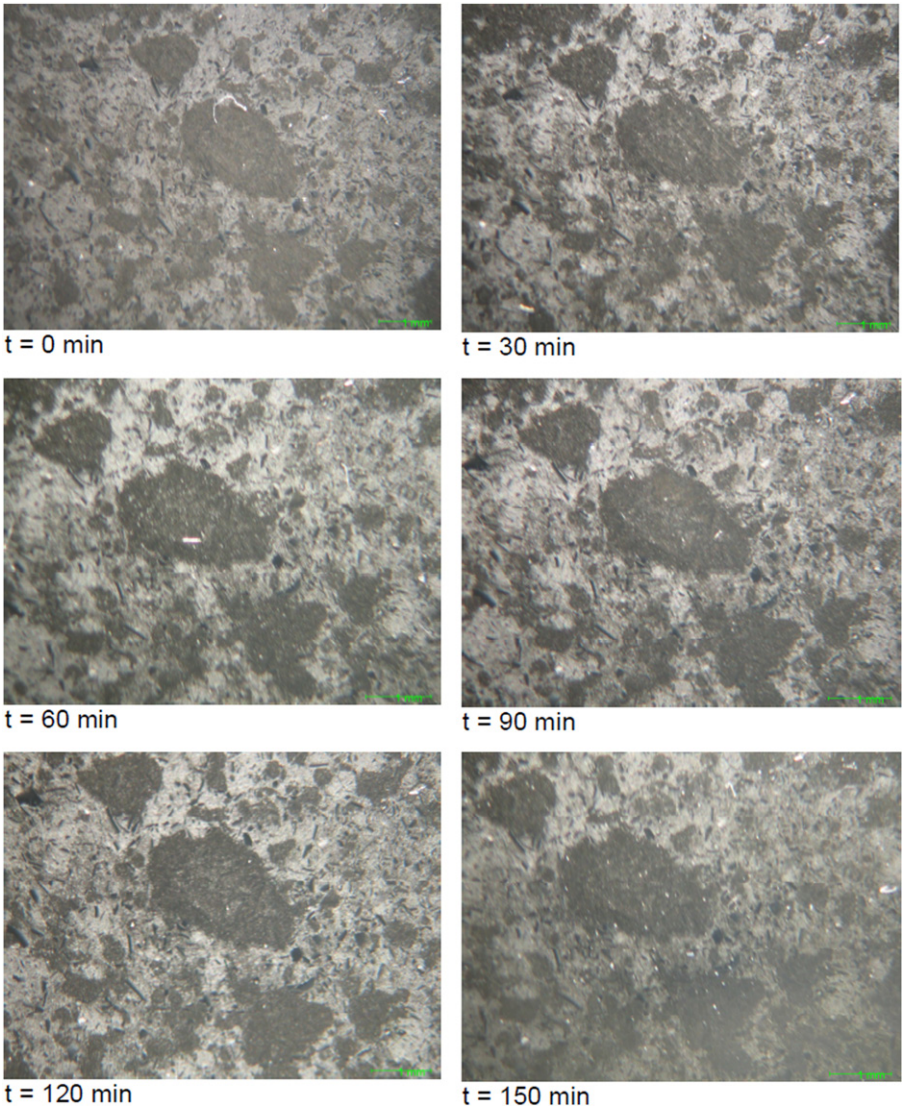

Fig. 11. Macrophotographs of the sample surface during cavitation testing.

According to the results obtained during the cavitations erosion testing, SPS composite could be a promising candidate for application as a cavitations erosion resistant material.

The results of microhardness, fracture toughness, density, cavitations erosion testing and the surface analysis of the SPS composite, show that this material can be applied as a structural ceramics in very aggressive environments.

Acknowledgment

This project was financially supported by the Serbian Ministry of Education and Science on projects 45005 and 45012. Special thanks to Dr. Vladimir Pavlović, Dr. Miodrag Mitrić and Dr. Zlatko Rakočević for their contribution in this work, done by SEM imaging, XRD and AFM analysis, respectively. The authors are grateful to Prof. Dr. Markus Winterer, University of Duisburg–Essen, Germany for providing the SPS facility.

References

[1] H.O. Pierson, Handbook of Refractory Carbides and Nitrides, William Andrew Publishing&Noyes, Westwood, NJ, 1996, pp. 68.
[2] H.J. Ryu, Y.W. Lee, S.I. Cha, S.H. Hong, Sintering behaviour and microstructure of carbides and nitrides for the inert matrix fuel by spark plasma sintering, Journal of Nuclear Materials 352 (2006) 341–348.
[3] E. Min-Haga, W.D. Scott, Sintering and mechanical properties of ZrC–ZrO_2 composites, Journal of Materials Science 23 (1988) 2865–2870.
[4] W.G. Fahrenholtz, G.E. Hilmas, I.G. Talmy, J.A. Zaykoski, Refractory diborides of zirconium and hafnium, Journal of the American Ceramic Society 90 (2007) 1347–1364.
[5] M.M. Opeka, I.G. Talmy, W.J. Wuchina, J. Zaykoski, S.J. Causey, Mechanical, thermal, and oxidation properties of refractory hafnium and zirconium compounds, Journal of the European Ceramic Society 19 (1999) 2405–2414.
[6] M. M. Schwartz, Handbook of Structural Ceramics, McGraw-Hill, New York, 1992.
[7] S.Q. Guo, J.M. Yang, H. Tanaka, Y. Kagawa, Effect of thermal exposure on strength of ZrB_2-based composites with nano-sized SiC particles, Composites Science and Technology 68 (2008) 3033–3040.
[8] K.H. Kim, K.B. Shim, The effect of lanthanum on the fabrication of ZrB_2–ZrC composites by spark plasma sintering, Materials Characterization 50 (2003) 31–37.
[9] T. Tsuchida, S. Yamamoto, MA-SHS and SPS of ZrB2–ZrC composites, Solid State Ionics 172 (2004) 215–216.
[10] U. Anselmi-Tamburini, Y. Kodera, M. Gasch, C. Unuvar, Z.A. Munir, M. Ohyanagi, S.M. Johnson, Synthesis and characterization of dense ultra-high temperature thermal protection materials produced by field activation through spark plasma sintering (SPS): I. Hafnium Diboride,,, Journal of Materials Science 41 (10) (2006) 3097–3104.
[11] D. Scitti, S. Guicciardi, M. Nygren, Sparc plasma sintering and mechanical behavior of ZrC-based composites, Scripta Materialia 59 (2008) 638–641.
[12] T. Nishimura, M. Mitomo, H. Hirotsuru, M. Kawahara, Fabrication of silicon nitride nano-ceramics by sparc plasma sintering, Journal of Materials Science Letters (1995) 1046–1047.
[13] L. Bowen, T. Carruthers, R. Brook, Hot-pressing of Si_3N_4 with Y_2O_3 and Li_2O as additives, Journal of the American Ceramic Society 61 (7–8) (1978) 335–339.
[14] B. Matovic, G. Rixecker, F. Aldinger, Pressureless sintering of silicon nitride with lithia and yttria, Journal of the European Ceramic Society 24 (2004) 3395–3398.
[15] K. Watari, M. Valecillos, M. Brito, M. Toriyama, S. Kanzaki, Densification and thermal conductivity of AlN doped with Y_2O_3, CaO, and Li_2O, Journal of the American Ceramic Society 79 (1996) 3101–3108.
[16] Lj. Kljajević, B. Matović, A. Radosavljević-Mihajlović, M. Rosić, S. Bosković, A. Devečerski, Preparation of ZrO_2 and ZrO_2/SiC powders by carbothermal reduction of $ZrSiO_4$, Journal of Alloys and Compounds 509 (2011) 2203–2215.
[17] B. Matovic, G. Rixecker, F. Aldinger, Densification of Si_3N_4 with $LiYO_2$ additive, Journal of the American Ceramic Society 87 (2004) 546–549.
[18] G.R. Anstis, P. Chantikul, B.R. Lawn, D.B. Marshall, A critical evaluation of indentation techniques for measuring fracture toughness: i, direct crack measurements, Journal of the American Ceramic Society 64 (1981) 533–538.
[19] S. Martinović, J. Majstorović, V. Vidojković, T. Volkov-Husović, Influence of the damage level during quenching on thermal shock behavior of low cement castable, Science of Sintering 42 (2010) 211–219.
[20] R. Garcia, R. Magerle, R. Perez, Nanoscale compositional mapping with gentle forces, Nature Materials 6 (2007) 405–411.
[21] B. Anczykowski, B. Gotsmann, H. Fuchs, J.P. Cleveland, V.B. Elings, How to measure energy dissipation in dynamic mode atomic force microscopy, Applied Surface Science 140 (1999) 376–382.
[22] T. Tamayo, R. Garcia, Deformation, contact time and phase contrast in tapping mode scanning force microscopy, Langmuir 12 (1996) 4430–4435.
[23] P.J. James, M. Antognozzi, J. Tamayo, T.J. McMaster, J.M. Newton, M.J. Miles, Interpretation of contrast in tapping mode AFM and shear force microscopy—a study of nafion, Langmuir 17 (2001) 349–360.
[24] G.G.A. Fatjo', M. Hadfield, C. Vieillard, J. Sekulić, Early stage cavitation erosion within ceramics—an experimental investigation, Ceramics International 35 (2009) 3301–3312.
[25] T. Okada, Y. Iwai, S. Hattori, N. Tanimura, Relation between impact load and the damage produced by cavitation bubble collapse, Wear 184 (2) (1995) 231–239.
[26] M. Dojčinović, T. Volkov-Husović, Cavitation damage of the medium carbon steel: implementation of image analysis, Materials Letters 62 (2008) 953–956.
[27] M. Dojčinović, S. Marković, The morphology of cavitation damage of heattreated medium carbon steel, Journal of the Serbian Chemical Society 71 (8-9) (2006) 977–984.
[28] G. Bregliozzi, A. Di Schino, S.I.-U. Ahmed, J.M. Kenny, H. Haefke, Cavitation wear behaviour of austenitic stainless steels with different grain sizes, Wear 258 (1-4) (2005) 503–510.
[29] W.J. Tomlinson, A.S. Bransden, Cavitation erosion of laser surface alloyed coatings on Al–12%Si, Wear 185 (1995) 59–65.
[30] C.J. Lin, J.L. He, Cavitation erosion behaviour of electroless nickel-plating on AlSl 1045 steel, Wear 259 (1-6) (2005) 154–159.
[31] S. Martinović, M. Vlahović, M. Dojčinović, T. Volkov-Husović, J. Majstorović, Thermomechanical properties and cavitation resistance of a high-alumina low-cement castable, International Journal of Applied Ceramic Technology (2010)http://dx.doi.org/10.1111/j.1744-7402.2010.02545.x.
[32] S. Martinović, M. Dojcinović, M. Dimitrijević, A. Devečerski, B. Matović, T. Volkov-Husovic, Implementation of image analysis on thermal shock and cavitation resistance testing of refractory concrete, Journal of the European Ceramic Society 30 (16) (2010) 3303–3309.
[33] M. Nagura, A. Suzuki, K. Sasaki, T. Terai, Chemical stability of $LiYO_2$ as an insulating material, Fusion Engineering and Design 85 (2010) 1098–1101.

[34] S. Strbac, M. Nenadovic, Lj. Rajakovic, Z. Rakocevic, Chemical surface composition of the polyethylene implanted by Ag^+ ions studied by phase imaging atomic force microscopy, Applied Surface Science 256 (2010) 3895–3899.
[35] S.N. Magonov, V. Elings, M.H. Whangbo, Phase imaging and stiffness in tapping mode atomic force microscopy, Surface Science 375 (1997) L385–L391.
[36] E. Min-Haga, W.D. Scott, Sintering and mechanical properties of ZrC–ZrO_2 composites, Journal of Materials Science 23 (1998) 2865–2870.
[37] K. Upadhya, J.M. Yang, W.P. Hoffmann, Materials for ultrahigh temperature structural applications, American Ceramic Society Bulletin 58 (1997) 51–56.